RESEARCH ARTICLE

Sediment erodibility in the Changjiang (Yangtze) subaqueous delta: spatial–temporal distribution and sedimentary significance

Chaoran Xu[1], Dongyun Wei[1], Yining Chen[2], Yang Yang[3], Fan Zhang[1], Ya Ping Wang[1] and Jianjun Jia[1,2,4*]

Abstract

Delta evolution in the context of no sediment discharge has become a global concern, and an accretion-to-erosion conversion is occurring in the Yangtze estuary. This conversion could threaten Changjiang subaqueous delta development. Sediment erodibility is an important indicator of subaqueous delta vulnerability. However, the present and future erodibility of the Changjiang subaqueous delta remains unclear. In this study, 37 short cores were collected from the Changjiang subaqueous delta, and the critical shear stress of the sediment was measured using a cohesive strength meter (CSM) and compared with estimates based on an empirical Shields diagram. The sediment erodibility was analyzed by comparing the sediment critical shear stress with the bed shear stress simulated using a numerical model (i.e., FVCOM), and sediment activity was introduced to discuss the geomorphological change in the subaqueous delta. The CSM-derived critical shear stress is significantly higher than that derived from the empirical Shields formula, but it better shows the erodibility of the sediment. The annual surface sediment activity ranges from 5% to 30% based on the CSM, indicating low surface erodibility. Moreover, the critical shear stress in this region increases as water depth increases, but the bed shear stress shows the opposite trend. Therefore, the erodibility of the Changjiang subaqueous delta is lower than that of the shallow area, indicating no accretion-erosion conversion or continued vertical erosion under sediment starvation in the coming decades. These findings can provide suggestions for erosion assessment and management in large river deltas under decreasing sediment discharge.

Keywords: Sediment erodibility, Changjiang subaqueous delta, Cohesive strength meter, Critical shear stress, Sediment activity

1 Introduction

River deltas, some of the most active areas of deposition on Earth, are formed by the accumulation of terrestrially derived sediments (Wright 1977). The evolution of deltas has played an important role in the development of human society and holds both socioeconomic and environmental significance because of the dense population and diverse ecosystems that they host (Syvitski and Saito 2007). However, in recent decades, the development of deltas has been threatened by a dramatic decrease in sediment discharge due to human activities, such as dam construction, soil and water conservation, and climate change (Syvitski et al. 2005; Giosan et al. 2014). Thus, the evolution of subaqueous deltas lacking fluvial sediment supply has become a global concern (Luo et al. 2017; Yang et al. 2021; Day et al. 2016). The Changjiang River, the third-largest river in the world, has faced a large decline in sediment discharge in recent decades (Yang et al. 2015), which will cause erosion of the subaerial delta, leading to the retreat of the coastline, and may affect the accretion and erosion processes of the Changjiang subaqueous delta (CSD) (Syvitski et al. 2009). Sediment erodibility is an important indicator of subaqueous

*Correspondence: jjjia@sklec.ecnu.edu.cn

[2] State Research Centre for Island Exploitation and Management, Second Institute of Oceanography, MNR, Hangzhou 310012, China
Full list of author information is available at the end of the article

delta vulnerability; however, the present and future erodibility of the Changjiang subaqueous delta in the context of a lack of sediment supply is not well understood.
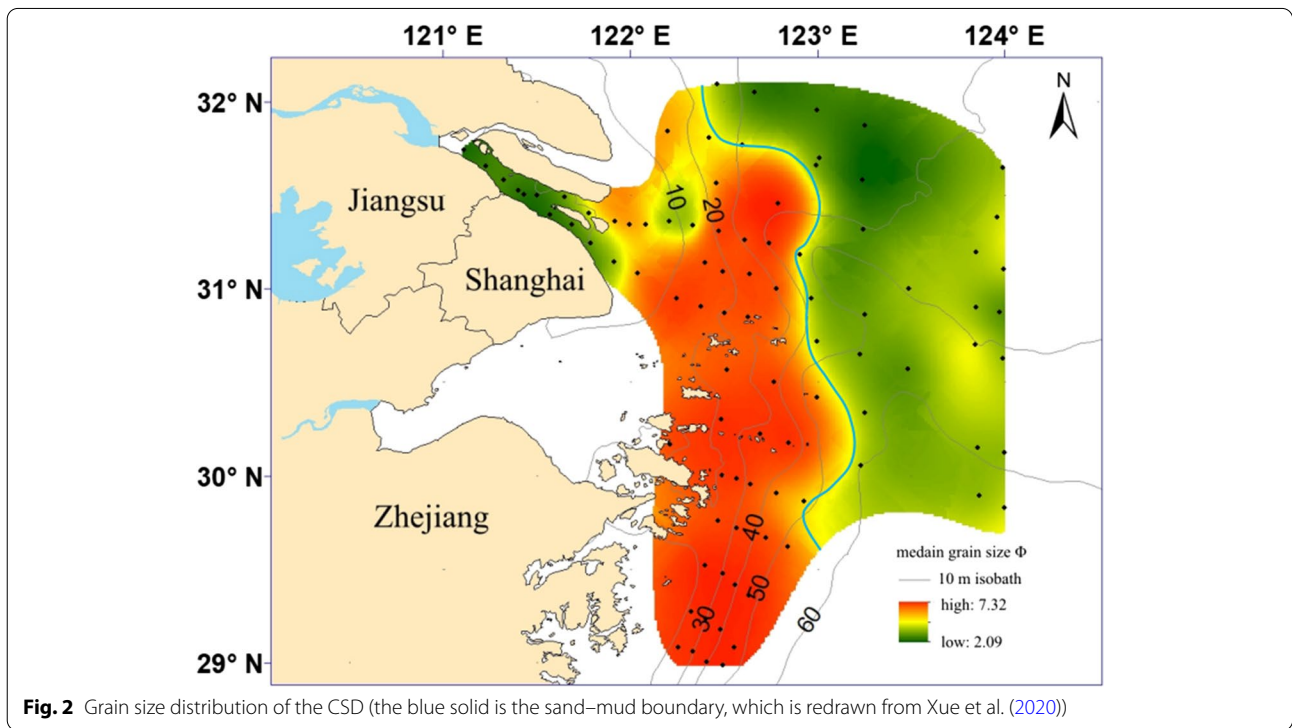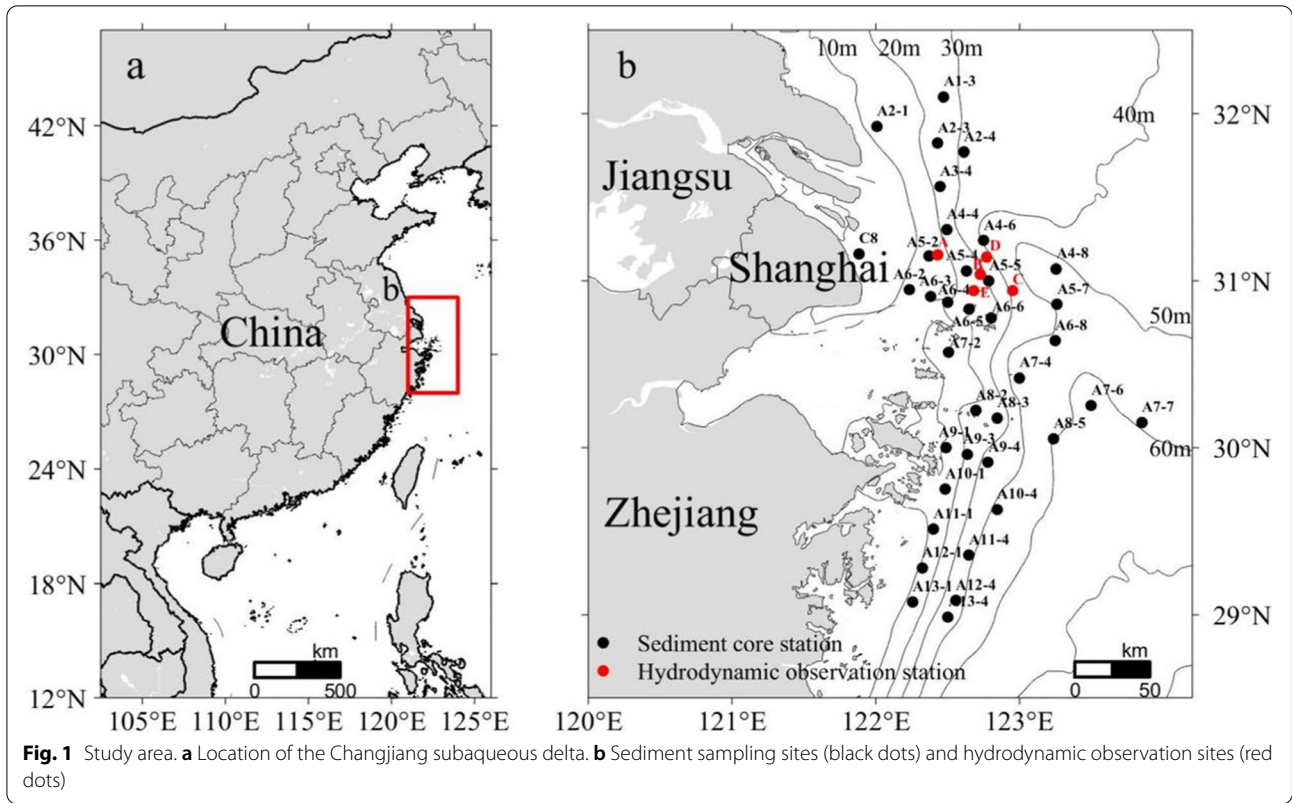
The Changjiang River originates from the Qinghai-Tibet Plateau and flows 6300 km eastward to the East China Sea, ranking fourth in sediment transport and fifth in water discharge (Milliman and Farnsworth 2011; Milliman et al. 1985), and more than 450 million people live in the Changjiang River basin (Yang et al. 2015). After the Three Gorges Dam was established, the sediment discharge in the Changjiang River was reduced by more than 70% (Yang et al. 2015). Will such a massive loss of sediment discharge lead to the erosion of the CSD, similar to the erosion of the Mississippi and Colorado Rivers, due to reduced sediment discharge (Maloney et al. 2018; Carriquiry et al. 2001)? Some previous studies have used nautical charts or performed field bathymetric measurements to establish a digital elevation model (DEM) using bathymetric data and found that the Changjiang mouth bar area, which is shallower than 10 m isobaths, is experiencing an accretion-to-erosion conversion (Luan et al. 2021; Li et al. 2015). However, such studies are limited by the amount of data, mostly focus on areas shallower than 20 m isobaths, and are limited to studying and analyzing the surface layer. On the other hand, sediment erosion, transport, and redistribution are related to the threshold of sediment motion, and the sediment critical shear stress τ_{cr} is used mostly to quantify the threshold of sediment motion (Yang et al. 2019). Therefore, the combined analysis of hydrodynamic and sediment motion is also a common method to analyze the accretion and erosion processes. Sediment activity, which is the percentage of time when surficial seafloor sediments are in motion during a given period, is determined by a combination of sediment properties, critical shear stress τ_{cr} and the hydrodynamic process under which it is located and can be used to express the accretion and erosion processes (Gao et al. 2001). Yang et al. (2017) analyzed the relationship between the hydrodynamic process in the CSD and the critical shear stress of sediment calculated using an empirical formula and concluded that future vertical erodibility of the CSD is inevitable. However, the threshold of motion is related to the grain Reynolds number, grain size distribution, sphericity, roundness, cohesiveness, and turbulence (Yang et al. 2019). The commonly used empirical formula to calculate the critical shear stress τ_{cr-f} method for sediments does not reflect the real situation, and the field flume experiment has less application because of the complicated setup. Therefore, a device for measuring the critical shear stress, namely, a cohesive strength meter (CSM), has been widely used for field and laboratory measurements of critical shear stress in sediments due to its portability, short test time, and small sample requirement (Tolhursta et al. 1999; Chen et al. 2012; Tolhurst et al. 2000; Mai et al. 2022; Liu et al. 2017).

Sediment stability is determined by the balance between erosive and resistive forces. The principal erosive forces are shear stress and turbulence on the sediment surface from flowing water, as well as solid transfer stress from particles moving along the substrate bed (Amos et al. 2004). These forces are counteracted by forces in the sediment that resist erosion, including gravity, friction, cohesion, and adhesion, and these resistances are represented by erodibility, which is usually expressed as the erosion threshold or erosion rate (Sanford 2008). The erosion threshold can be represented by the sediment critical shear stress, as mentioned above. Therefore, in this study, a box sampler was used to collect short sediment cores from the CSD to extend the erodibility analysis to a water depth of 60 m. A CSM was used to measure the surface and vertical critical shear stress to obtain the spatial and vertical critical shear stresses. The critical shear stresses were also calculated using empirical formulas to analyze the differences between the two methods. Moreover, the sediment activity was calculated by combining the bed shear stress τ_b simulated by the Finite-Volume Coastal Ocean Model (FVCOM) to analyze the present and future erodibility of the CSD.

2 Materials and methods
2.1 Study area
The study area is the CSD between water depths of 10 m and 60 m (Fig. 1). The progradation of the Changjiang delta spans more than 200 km, and the sedimentation thickness has exceeded 60 m since the middle Holocene; the progradation has accelerated in the last 2000 years due to human activities on the watershed (Hori et al. 2001). Now, the CSD covers an area of approximately 10,000 km², with flat topography. The current Changjiang mouth has four outlets, and more than 95% of the Changjiang's water and sediment flows into the sea via the three outlets of the South Branch (Dai et al. 2016). As shown in Fig. 2, the grain size components of the North Branch and South Branch are dominated by sandy silt, the mouth bar area and adjacent subaqueous are dominated by mud, and the area to the east of 123°E is dominated by silty sand (Xue et al. 2020). The astronomical tide around the CSD is irregular and semidiurnal, with mean and maximum tidal ranges of 2.66 and 4.62 m, respectively (Yun 2004). The wind speed in this area is highly variable, with a multiyear average wind speed of 4-5 m/s and a maximum wind speed of 36 m/s (Shi et al. 2014). The annual water discharge (1950-2020) of the Datong station (tidal limit) was 898 km³ yr⁻¹, and the water discharge was 1118 km³ yr⁻¹ in 2020; the annual sediment discharge was 351 Mt yr⁻¹, and the sediment discharge was 164 Mt yr⁻¹ in 2020 (CWRC 2021). The river water and sediment discharge have strong seasonal variations, with approximately 71% of the annual

Fig. 1 Study area. **a** Location of the Changjiang subaqueous delta. **b** Sediment sampling sites (black dots) and hydrodynamic observation sites (red dots)

Fig. 2 Grain size distribution of the CSD (the blue solid is the sand–mud boundary, which is redrawn from Xue et al. (2020))

runoff and 87% of the annual sediment load delivered to the mouth during the flood season from May to October (Chen et al. 2007). The water discharge of the Changjiang River has not changed much in recent decades, while the sediment discharge has decreased significantly.

2.2 Data source

We collected sediment samples in October 2019 and July 2020 aboard the scientific research vessel organized by the National Natural Science Foundation of China (NSFC). Thirty-seven sediment cores (lengths vary from 20 to 50 cm; sediment sampling sites are shown in Fig. 1b, of these, 34 sediment cores were collected in October

$$\tau_{cr-m} = 66.6734 \times \left[1 - e^{\left(-\frac{P}{310.09433} \right)} \right] - 195.27552 \times \left[1 - e^{\left(-\frac{P}{1622.556738} \right)} \right] \tag{1}$$

2019 and 3 sediment cores were collected in July 2020) were collected by a box sampler and extracted by hand using an acrylic core tube (7.5 cm diameter), ensuring an undisturbed sediment surface and a consistent depth of overlying water for subsequent erodibility measurements. Moreover, we collect 37 sediment from the top layer (0-5 cm) of the box sampler as the surface sediment.

2.3 Experiment and data processing
2.3.1 Grain size analysis
We used all of the surface sediment samples and 2 cm subsamples of 10 short cores near the Yangtze Estuary (A2-1, A2-4, A4-4, A4-6, A4-8, A6-2, A6-4, A6-5, A6-6, and A6-8) to measure these grain sizes. Prior to grain size analysis, we used 0.5 mol/L of (NaPO3)6 to disperse the sediment samples for 24 hours, and then mixed them evenly with ultrasound (15 s). Fiannly, we used a laser particle analyzer (Mastersizer 2000, United Kingdom) for grain size analysis. It has a measurement range of 0.02–2000 μm with a relative error of <3% for repeated measurements. The resulting median grain size of the sediment was obtained and used for subsequent calculations of the critical shear stress based on the empirical formula.

2.3.2 CSM-derived critical shear stress τcr − m
This study used the cohesive strength meter (CSM, MKIV, Partrac, Britain) (Tolhursta et al. 1999) to measure the sediment critical shear stress. It consists of three principal parts (Fig. S2): a controller, which controls the test process and logs the data; a pneumatic and hydraulic pipe system; and a head sensor chamber fitted with infrared optics. The pipe system connects with the chamber to form a vertical water jet. The test chamber was placed onto the surface sediment by pushing it flush onto the surface before the test, giving

a footprint of 6.6 cm² (Tolhursta et al. 1999). The CSM employs a jet of pressurized water to determine the critical shear stress of the sediment. By sequentially increasing the force of the jet, the initial point erosion can be determined by the associated reduction in light transmission across a test chamber as sediment is entrained in suspension. When the light transmission decreases by more than 5% compared to the initial state (from 100% to 95%), the sediment is resuspended at this time, and the controller shows the critical pressure P (psi) (Tolhursta et al. 1999). After converting the units of P to kPa, the critical pressure is subsequently converted to critical shear stress τ_{cr-m} (N/m²), according to Eq. (1) (Tolhursta et al. 1999).

Water depths in the sea exceeded the manufacturer's guidelines, so the CSM could not be used in situ. Therefore, the critical shear stress was measured within the sediment core tubes (Section 2.2). The sediment core tubes were first placed vertically, and the test chamber was placed into the surface sediment samples to measure the surface critical shear stress. Then, the cores were split into two parts using a GeoTek Core Splitter. One-half of the core was used to measure the vertical critical shear stress with a measurement spacing of 5 cm.

2.3.3 Empirical formula-derived critical shear stress τcr − f
Guo (2020) applies the Padé approximant to the data in the extended Shields diagram and presents a simple generalized empirical model for the critical shear stress. The minimum applicable median grain size of this curve is 4 μm (Fig. S1), the proposed function results in an explicit Shields diagram in terms of the grain Reynolds number and has an analytical solution for the critical sediment diameter given a bed shear stress. Although the Shields diagram considers no-cohesive sediments, this method extends its applicability to 4 μm, we therefore consider it applicable to the sediments in the present.syudy area. This study used this empirical model to calculate the sediment critical shear stress τ_{cr-f}:

$$\tau_{cr-f} = \tau_*(\gamma_s - \gamma)D \tag{2}$$

where γ_s is the sediment specific weight, γ is the water specific weight, D is the sediment median grain size, and τ_* is the critical Shields parameter and is denoted by Eq. (3):

$$\tau_* = \frac{R_*^2}{D_*^3} \tag{3}$$

where D_* is the dimensionless sediment diameter defined by Eq. (4), and R_* is the critical grain Reynolds number, which is denoted by Eq. (5):

$$D_* = D\left[\frac{(\Delta-1)g}{\nu^3}\right]^{\frac{1}{3}} \tag{4}$$

where $\Delta = \frac{\gamma_s}{\gamma}$ is the specific gravity, ν is the kinematic water viscosity, and g is the gravitational acceleration.

$$R_*^4 + \frac{195}{7}R_*^3 + \left(\frac{162}{7} - \frac{D_*^3}{18}\right)R_*^2 - \frac{11}{12}D_*^3 R_* - \frac{81}{14}D_*^3 = 0 \tag{5}$$

Equation (5) can be solved analytically by applying the quartic roots formula, and the maximum real root is R_*.

2.3.4 FVCOM-derived bed shear stress τb

The three-dimensional finite-volume coastal ocean model (FVCOM) was used to simulate the hydrodynamics of the CSD. FVCOM is a finite-volume, free-surface, and primitive-equations community ocean model, and the unstructured triangular grid adopted in FVCOM is suitable for the complex coastline of coastal estuaries and is widely used in the study of estuarine coastal hydrodynamic processes (Chen et al. 2006). The model domain covers the shelf estuary of the East China Sea region, and the maximum and minimum grid sizes of the meshes are 10,000 m at the open boundary and 100-400 m nearshore. The tides at the ocean open boundary were derived from TPXO9. The bottom roughness lengths were set as 0.1-5 mm concerning the spatial distribution of the bottom sediment grain size. Wind field data from the Climate Forecast System Reanalysis (CFSR) were applied to the model domain. The three-dimensional initial salinity and temperature field and initial bathymetric data were taken from the Global Hybrid Coordinate Model (HYCOM). The model results of elevation and current were validated against the hydrodynamic data from a field trip in July 2019. The model can better simulate the hydrodynamic situation of the CSD, and the validation of the model is shown in Figs. S3 & S4.

The bed shear stress in the FVCOM is calculated by Eq. (6):

$$\overrightarrow{\tau_b} = \rho C_d \left|\overrightarrow{u_b}\right|\overrightarrow{u_b} \tag{6}$$

where ρ is the density of seawater, u_b is the bottom ($z = z_b$) current velocity, and C_d is the bottom drag coefficient in a sediment-laden bottom boundary layer, as given by Eq. (7):

$$C_d = \max\left\{\left[\frac{1}{k}\ln\left(\frac{z_b}{z_0}\right)\right]^{-2}, 0.0025\right\} \tag{7}$$

where z_0 is the bottom roughness length, z_b is the position of the near-bottom sigma layer below the water surface, and k is the Von Karman constant (0.4) (Chen et al. 2006). Then, the hour-by-hour bed shear stress τ_b was obtained for 37 sites from January 1, 2019, to December 31, 2019.
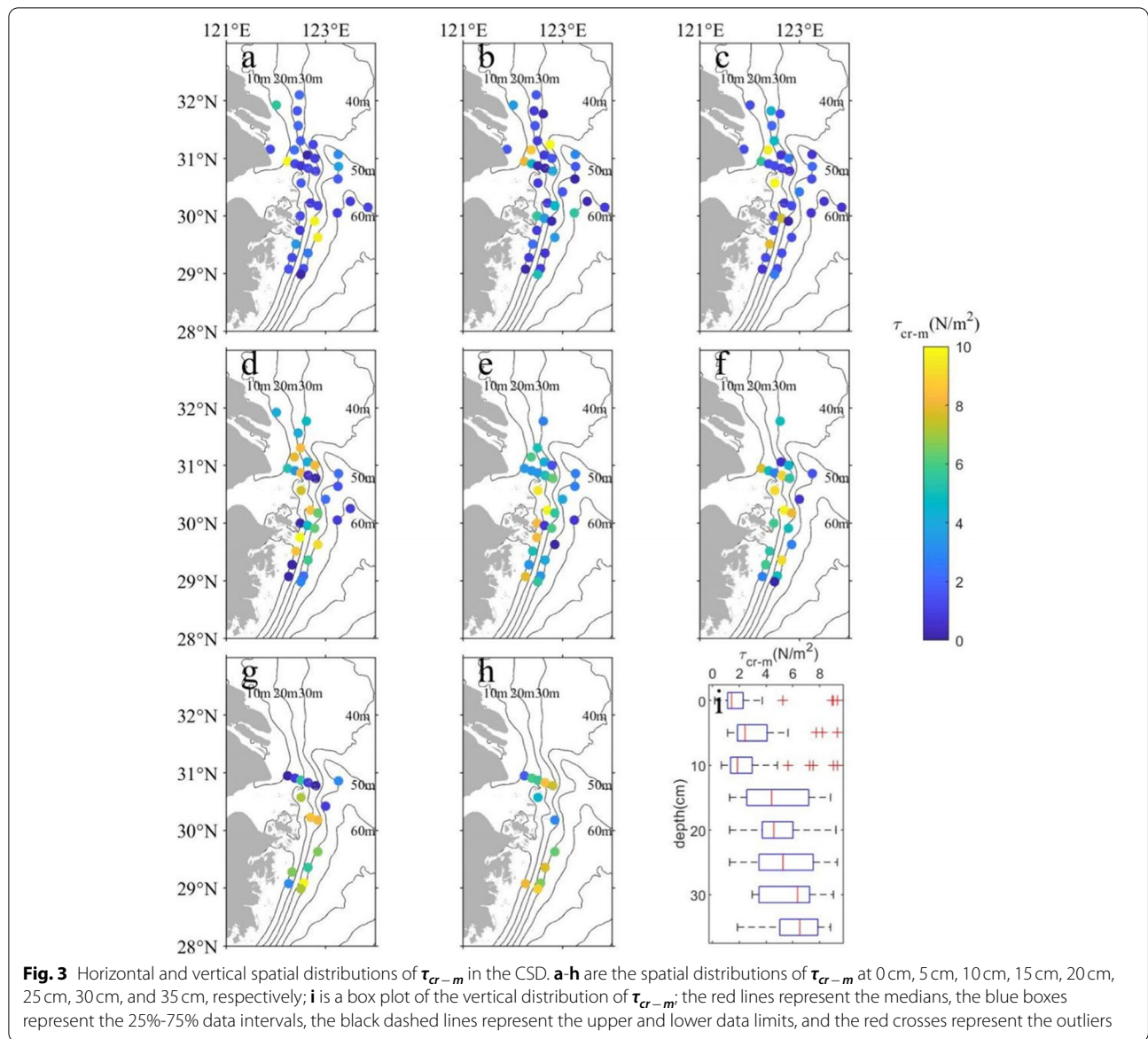
3 Results

3.1 CSM-derived τ_{cr-m}

The short sediment cores collected by the box sampler are mostly within 30 cm, and a few exceed 35 cm. Therefore, the analysis of τ_{cr-m} in this study focused on the upper 35 cm. The τ_{cr-m} values of each layer are analyzed in both horizontal and vertical distributions. The τ_{cr-m} shows an overall trend of gradually increasing with depth, and the values on the southwest side are larger than those in the other regions (Fig. 3). As shown in Fig. 3i, the τ_{cr-m} values fluctuate less in the upper region of 0-10 cm, the values in the 0 cm layer vary mainly from 1.11-2.28 N/m^2, those in the 5 cm layer vary mainly from 1.86-4.06 N/m^2, those in the 10 cm layer vary mainly from 1.34-2.95 N/m^2, and the standard deviations are 0.78, 1.38, and 0.89, respectively; the τ_{cr-m} values fluctuate more in the lower region of 15-35 cm, the values in the 15 cm layer vary mainly from 2.55-7.18 N/m^2, those in the 20 cm layer vary mainly from 3.07-6.00 N/m^2, those in the 25 cm layer vary mainly from 3.47-7.51 N/m^2, those in the 30 cm layer vary mainly from 3.46-7.25 N/m^2, those in the 35 cm layer vary mainly from 5.02-7.86 N/m^2, and the standard deviations are 2.39, 2.00, 2.34, 1.98, and 2.10, respectively. These results indicate that the τ_{cr-m} values in the upper layer have low spatial heterogeneity, while the τ_{cr-m} values in the lower layer have high spatial heterogeneity.

Since the τ_{cr-m} shows spatial heterogeneity, we grouped them according to water depth to observe the vertical variations in different regions. As shown in Fig. 4a-h, the τ_{cr-m} values in different regions show a decreasing trend with increasing depth, but the surface fluctuation in the same region is more obvious. Therefore, we conducted a unified analysis of the τ_{cr-m} values at 10 cm on the surface of each region and found obvious regional characteristics (Fig. 4i). These values fluctuate more in the region of shallow water depths of 15 m, while they fluctuate less in the region with water depths of 15 m-30 m. Then, the fluctuations suddenly increase at water depths of 30 m-50 m and decrease again at water depths of more than 50 m.

3.2 Empirical formula-derived τ_{cr-f}

The median grain sizes of the surficial sediment samples collected in this study range from 7 to 235 μm. The samples are dominated by silt, followed by clay, with the least amount of sand and with an average clay content of 15%. The overall τ_{cr-f} values calculated for this study area are small, from 0.03-0.25 N/m^2. Because the empirical formula relies only on the grain size to calculate τ_{cr-f}, the spatial distribution of τ_{cr-f} values is consistent with the grain size distribution in this region (Fig. 2), both of which have a spatial distribution pattern of low in the southwest and high in the northeast (Fig. 5a). Ten short sediment cores from the CSD (Fig. 5a) were selected for

Xu *et al. Anthropocene Coasts*   *(2022) 5:10*

Page 6 of 15

Fig. 3 Horizontal and vertical spatial distributions of τ_{cr-m} in the CSD. **a-h** are the spatial distributions of τ_{cr-m} at 0 cm, 5 cm, 10 cm, 15 cm, 20 cm, 25 cm, 30 cm, and 35 cm, respectively; **i** is a box plot of the vertical distribution of τ_{cr-m}; the red lines represent the medians, the blue boxes represent the 25%-75% data intervals, the black dashed lines represent the upper and lower data limits, and the red crosses represent the outliers
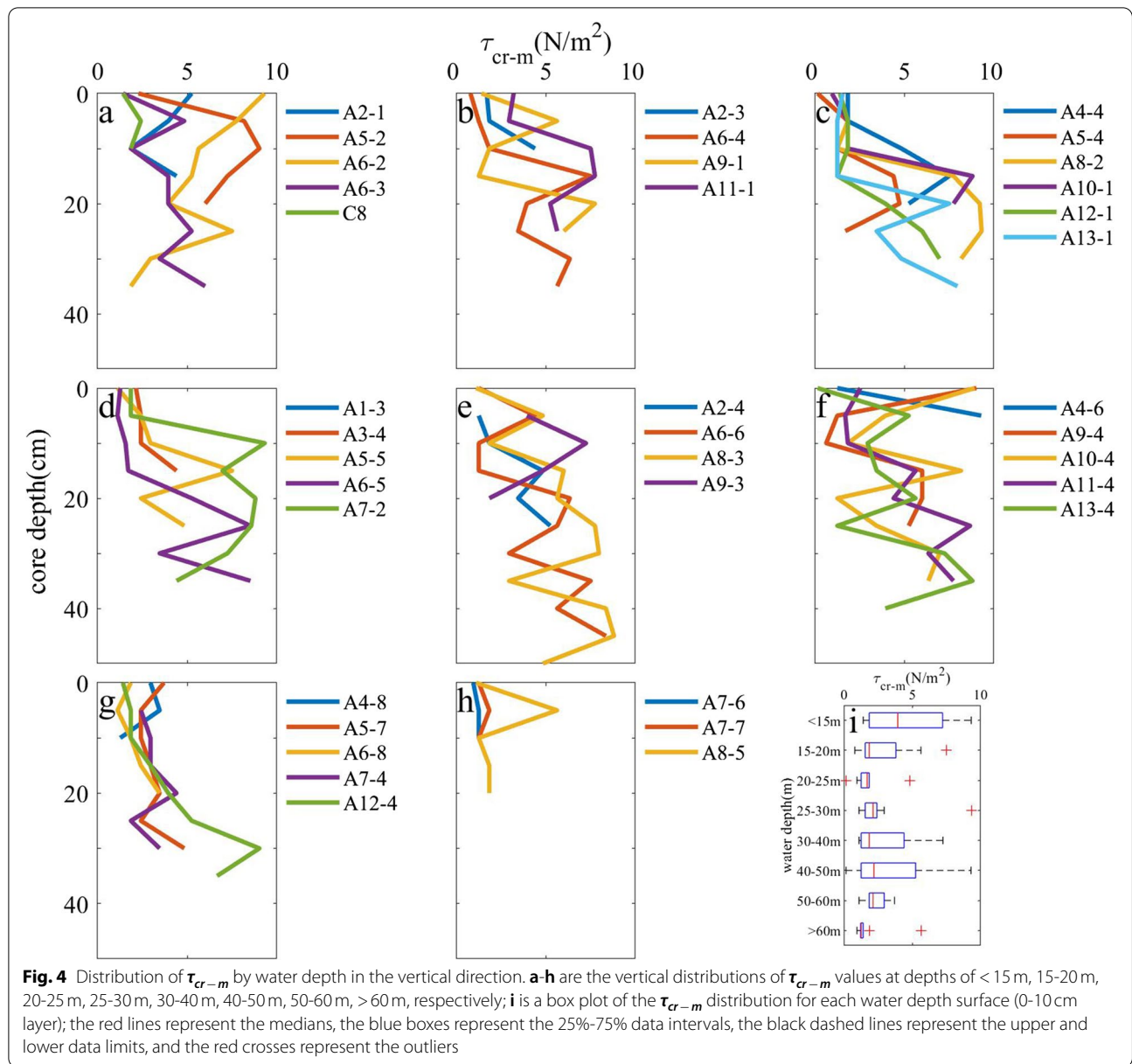
vertical grain size analysis. The sample sites were distributed throughout the northern part of the study area, near the adjacent subaqueous delta. The vertical trend of τ_{cr-f} values is not obvious, and the values are consistent with the surfaces. Since the surface sediments of the CSD show a coarsening trend (Yang et al. 2018), the grain sizes of some of the sediment core surface layers are larger than those of the lower layers, so τ_{cr-f} has a slight tendency to decrease with depth (Fig. 5b and c).

3.3 FVCOM-derived τ_b

The principal erosive forces are shear stress and turbulence imparted onto the sediment surface by flowing water

(Amos et al. 2004). Therefore, the bottom shear stress of the CSD is simulated in this study for subsequent comparison with the critical shear stress of the sediment. We simulated the hydrodynamic conditions of the CSD under normal conditions for the entirety of 2019 and calculated τ_b during all times of the year according to Eq. (6). The astronomical tide around the CSD is irregular and semidiurnal, and there are significant differences between the two consecutive semidiurnal tides. To analyze the variation in τ_b under tidal influence, two consecutive semidiurnal tides were treated as one semidiurnal tide in this study. The spring tide of October 2019 (2019/10/01/12:00-2019/10/02/13:00), the moderate tide of October 2019 (2019/10/04/04:00-2019/10/05/05:00), and the neap tide

Fig. 4 Distribution of τ_{cr-m} by water depth in the vertical direction. **a**-**h** are the vertical distributions of τ_{cr-m} values at depths of < 15 m, 15-20 m, 20-25 m, 25-30 m, 30-40 m, 40-50 m, 50-60 m, > 60 m, respectively; **i** is a box plot of the τ_{cr-m} distribution for each water depth surface (0-10 cm layer); the red lines represent the medians, the blue boxes represent the 25%-75% data intervals, the black dashed lines represent the upper and lower data limits, and the red crosses represent the outliers
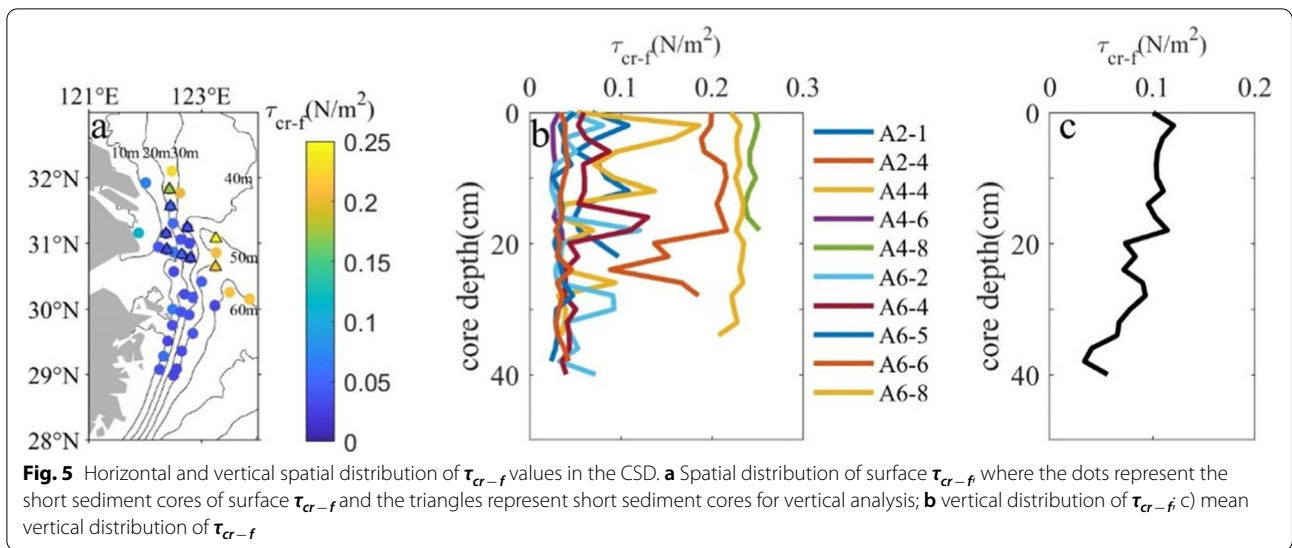
of October 2019 (2019/10/06/04:00-2019/10/07/05:00) were selected for analysis according to the tidal motion law and sampling time. The tidal current patterns for October 2019 are displayed in the Fig. S5 (Wei 2021). The bottom current during spring tide, moderate tide, neap tide, maximum flood and maximum ebb are 0.003-0.39 m/s, 0.004-0.36 m/s, 0.005-0.31 m/s, 0.03-1.11 m/s, 0-1.25 m/s, respectively. The results show that the annual τ_b values vary from 0.06-0.88 N/m^2, the mean τ_b values during spring tide vary from 0.11-1.39 N/m^2, the mean τ_b values during moderate tide vary from 0.06-0.81 N/m^2, and the mean τ_b values during neap tide vary from 0.03-0.41 N/m^2. The τ_b values

in the CSD are not large; the greater the tidal strength is, the greater the bottom shear stress. In addition, the values decrease as the water depth increases, while the values significantly decrease after a water depth of 30 m, with consistent changes in different periods; since the water depth of the CSD is shallow in the west and deep in the east, it is distributed in a strip, so the τ_b values show a spatial distribution of high in the west and low in the east (Fig. 6).

3.4 Sediment activity
Sediment activity is the percentage of the total time that the seafloor sediments are in motion during a given
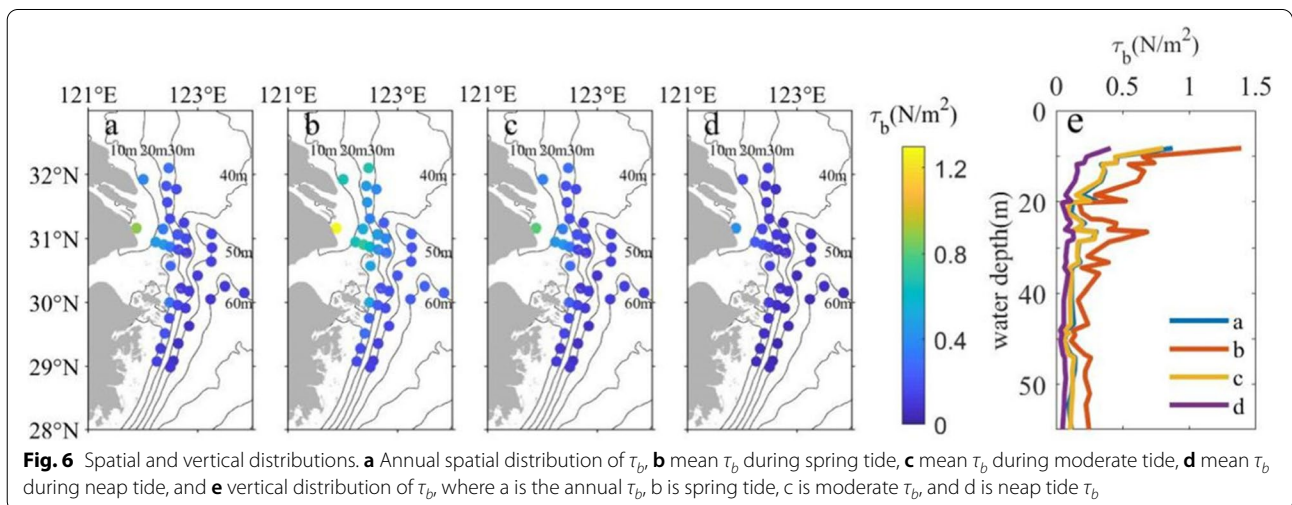
Fig. 5 Horizontal and vertical spatial distribution of τ_{cr-f} values in the CSD. **a** Spatial distribution of surface τ_{cr-f}, where the dots represent the short sediment cores of surface τ_{cr-f} and the triangles represent short sediment cores for vertical analysis; **b** vertical distribution of τ_{cr-f}; c) mean vertical distribution of τ_{cr-f}

period (Gao et al. 2001), as shown in Eq. (8). Sediment activity can be used to express the accretion-to-erosion conversion (Wei et al. 2021). Therefore, this study derives the erodibility of the sediments by analyzing the sediment activity. The CSM is a vertical jet-based device to measure τ_{cr}, although Tolhursta et al. (1999) used a theoretical calibrated formula to convert jet pressure to horizontal critical shear stress. Its determination of τ_{cr} is based on optical measurements of sediment resuspension. The sensor is positioned 1 cm from the sediment surface in the test chamber, and when erosion is measured, its measured τ_{cr} intensity is higher than the force required for the sediment to be eroded (Leeder 1999; Grabowski et al. 2010). Therefore, the CSM is best suited to relative measurements of erosion thresholds for cohesive sediment. The CSM can be compared longitudinally with devices with the same measuring principle and

cannot be compared directly with the horizontal shear stress (Vardy et al. 2007; Widdows et al. 2007).

$$sediment\ activity = \frac{sediment\ active\ time}{total\ time} \times 100\% \quad (8)$$

Laboratory and field flumes predominantly generate horizontal water flows across the sediment surface, and flumes produce controlled and well-understood hydrodynamic conditions, making them ideal for measuring critical shear stress τ_{cr} (Widdows et al. 2007). However, they are not as well-suited to investigate spatial and temporal variations in erodibility as the CSM and are difficult to use in the field. Grabowski et al. (2010) transformed the critical jet pressure P to the critical stagnation pressure P_{stag} according to a new theoretical calibrated formula, Eq. (9), by Vardy et al. (2007) and then proposing an empirical calibration, Eq. (10), between P_{stag} and the

Fig. 6 Spatial and vertical distributions. **a** Annual spatial distribution of τ_b, **b** mean τ_b during spring tide, **c** mean τ_b during moderate tide, **d** mean τ_b during neap tide, and **e** vertical distribution of τ_b, where a is the annual τ_b, b is spring tide, c is moderate τ_b, and d is neap tide τ_b

Xu *et al. Anthropocene Coasts* (2022) 5:10

Page 9 of 15

critical shear stress based on a comparison of erosion thresholds measured using the CSM and a laboratory flume. Grabowski et al. (2010) used sediment properties with clay contents of 5%-35% and median grain sizes of 60-200 μm, which are similar to the sediment properties in this study. Therefore, in the following, P (psi) is converted to τ_c according to Eqs. (9) and (10) and compared to τ_b to obtain the sediment activity for the subsequent discussion of the erodibility of the CSD.

$$P_{stag} = 3.47(6.89P)^{1.4} \qquad (9)$$

$$\tau_c = 0.0013P_{stag} + 0.047 \qquad (10)$$

The surface τ_c at each site was compared with τ_b for all periods of the year (January 1, 2019-December 31, 2019), as well as the spring tide period, moderate tide period, and neap tide period. When τ_b exceeded τ_c, the sediment was considered active, and the sediment activity time was compared with the total time to obtain the sediment activity. Similarly, the sediment activity of the empirical formula method was obtained from the above method (Fig. 7). The annual sediment activity values measured by the CSM vary from 4.38%-33.84%, the spring tide sediment activity values measured by the CSM vary from 42.31%-69.23%, the moderate tide sediment activity values measured by the CSM vary from 20.19%-64.42%, the neap tide sediment activity values measured by the CSM vary from 3.85%-42.31%, the annual sediment activity values calculated by the empirical formula vary from 68.89%-90.75%, the spring tide sediment activity values calculated by the empirical formula vary from 84.62%-96.15%, the moderate tide sediment activity values calculated by the empirical formula vary from 67.31%-96.15%, and the neap tide sediment activity values calculated by the empirical formula vary from 50.00%-80.77%.

4 Discussion

4.1 Difference between τ_{cr-m} and τ_{cr-f}

Due to consolidation (especially self-weight consolidation), the sediment is more stable (Fagherazzi and Furbish 2001), and the volume of the sediment is reduced due to self-weight after being covered with overlying sediment (Massey et al. 2006), which generally leads to downward consolidation with depth (Gehrels 1999). Therefore, τ_{cr-m} gradually increases as depth increases. Since the surface sediment is loose, the transport process
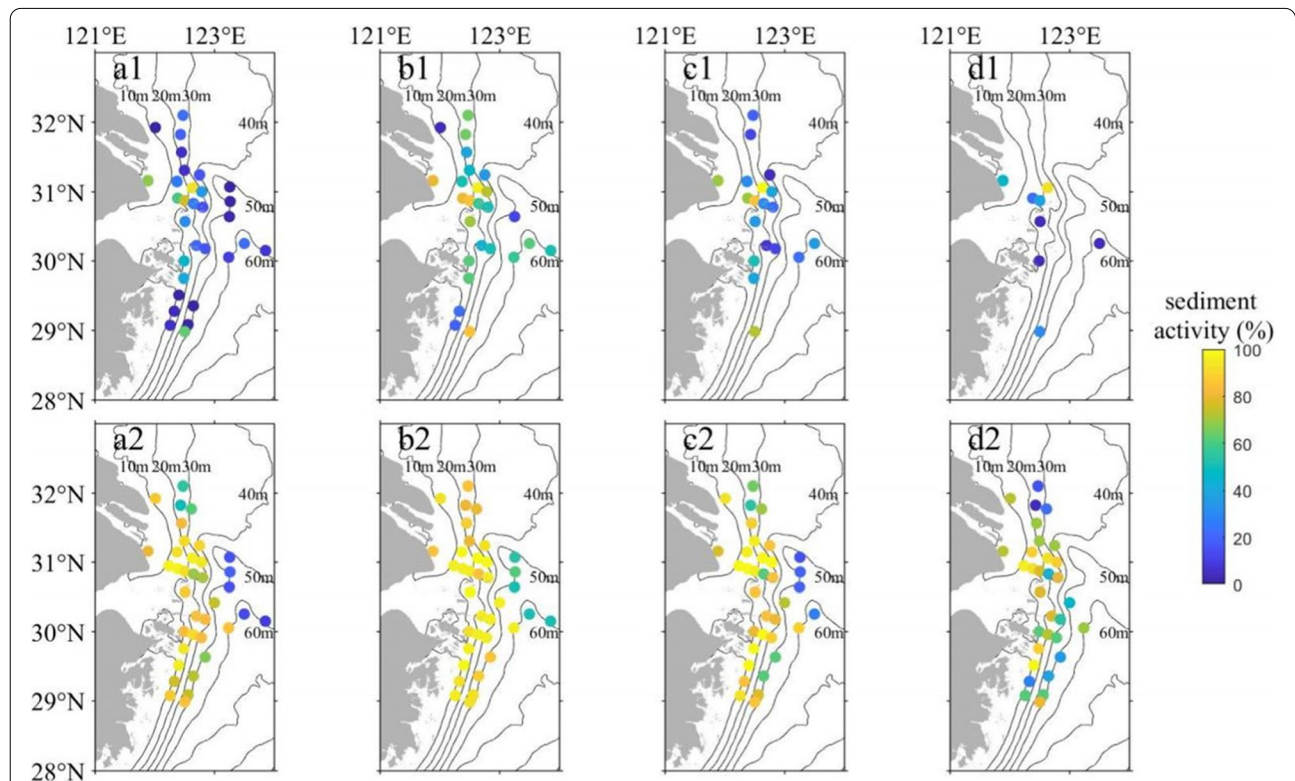

Fig. 7 Surface sediment activity in the CSD. **a** annual sediment activity, **b** spring tide sediment activity, **c** moderate tide sediment activity, **d** neap tide sediment activity; **1** is the CSM-measured sediment activity, and **2** is the empirical formula-measured sediment activity. If the sediment activity of a station is 0, the figure does not show the station

has some effect on the surface sediment, so the τ_{cr-m} of the surface sediment shows a small number of outliers, and the transport process does not have a significant effect on the CSM measurement results (Tolhurst et al. 2000). The τ_{cr-m} values within 0-10 cm at different water depths, as well as values in the interval from 15 m and shallower, fluctuate more because the bed shear stress due to the current is stronger the shallower the water depth is. In addition, the wave action is stronger in intervals of 20 m to shallow water depths, and the combined current–wave action normally leads to more disturbance of the surface sediment in shallow water. Therefore, more fluctuation occurs in shallow water. In areas with water depths of 30-50 m, τ_{cr-m} values suddenly fluctuate again. Figure 6e shows that the hydrodynamic conditions of the CSD change significantly after the water depth exceeds 30 m, while the sand–mud boundary (Fig. 2) of the CSD is in the range of 40-50 m and gradually recedes toward the shore (Luo et al. 2017). Therefore, the hydrodynamic and depositional environments in the 30-50 m region have changed considerably, which leads to larger fluctuations in the critical shear stress of the sediment.

The CSM-measured sediment activity shows a high central and low surrounding distribution, while the empirical formula-measured sediment activity changes similarly (Fig. 7). However, after a comparative analysis of the sediment activity calculated by τ_{cr-m} and τ_{cr-f} in the four periods, τ_{cr-m} differs from τ_{cr-f}. The CSM-measured sediment activity is significantly lower than the empirical formula-measured sediment activity (Fig. 8).

This result occurs because the critical shear stress of the sediment is influenced by several factors. It is not simple to predict the critical erosion shear stress of cohesive sediments from one or more easily measurable parameters, e.g., grain size, bulk density, water content, or organic content (Dade et al. 1992), and there are

differences compared to the real situation. Therefore, using field and laboratory measurements for τ_{cr} is accurate (Soulsby 1997; Whitehouse et al. 2000; Widdows et al. 2007). The CSM is widely used for measuring τ_{cr} due to its short test time, easily attainable equipment, and wide measurement range (Tolhursta et al. 1999). Both measurement methods indicate that the stronger the tide is, the higher the sediment activity. However, the annual sediment activity values of the empirical formula vary from 68.89%-90.75% (Fig. 8 a2). Even during the neap tide period when hydrodynamics are weak, the sediment activity values are 50.0%-80.77% (Fig. 8 d2), indicating that the surface sediments of the CSD are inactive most of the year if the empirical formula results are used. Moreover, τ_{cr-f} also has a tendency to decrease as depth increases, and the CSD will be fully eroded; some studies have shown that the CSD has a large area of erosion only in areas shallower than 10 m (Chen et al. 2018; Zhu et al. 2020; Luan et al. 2021), which is not consistent with the actual situation. The CSM-measured annual sediment activity values vary from 4.38%-33.84% (Fig. 8 a1), with a spatial distribution of high in the middle and low in the surrounding area. This pattern occurs because the sediments in the region west of 123°E are dominated by clayey silt and silt, and the grain size gradually increases from south to north (Fig. 2), with an average clay content of more than 15% (Xue et al. 2020). When the sediment clay content exceeds 4-10%, the τ_{cr} of the sediment is dominated by cohesive influence (Grabowski et al. 2010), and the τ_{cr} of the sediment under this condition tends to increase as grain size decreases (Dade et al. 1992). Therefore, the τ_{cr} in the southwest region is larger than that in the central region. The water depth of the CSD is distributed in a longitudinal strip with little difference between north and south; thus, the sediment activity in the southwest area (the mean annual sediment activity is 10.4%)
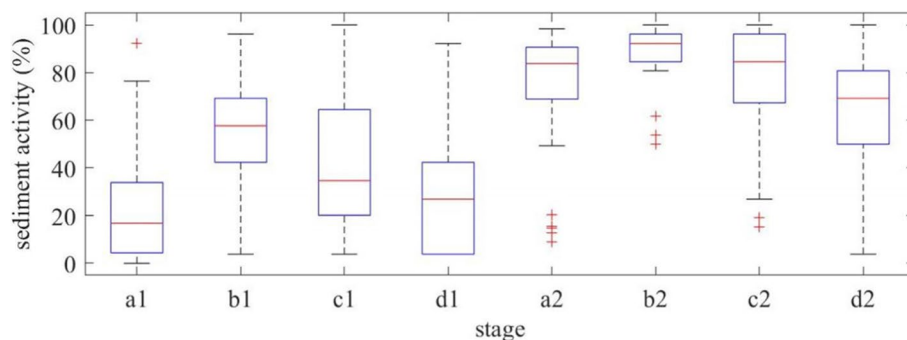

Fig. 8 Box plot of the sediment activity by period. **a** annual sediment activity, **b** spring tide sediment activity, **c** moderate tide sediment activity, **d** neap tide sediment activity; **1** is the CSM-measured sediment activity, and **2** is the empirical formula-measured sediment activity. The red lines represent the medians, the blue boxes represent the 25%-75% data intervals, the black dashed lines represent the upper and lower data limits, and the red crosses represent the outliers

is lower than that in the middle area (the mean annual sediment activity is 43.9%). The water depth in the east increases significantly, and we conclude in Section 3.3 that τ_b decreases significantly after a water depth of 30 m; thus, the sediment activity in the east is lower (the mean annual sediment activity is 21.9%).

The above results show that the CSM measurements are more consistent with the actual erodibility of the sediments and more accurately reflect the sediment activity in the CSD and adjacent sea. Therefore, we believe that the current surface layer of the CSD and adjacent sea is relatively stable and in an equilibrium state of erosion and siltation, and the erodibility is not high.

4.2 Future erodibility

We compare τ_c with τ_b for each layer to obtain the sediment activity in the vertical direction. Then, we analyze the ability of the lower sediment to be continuously activated after the surface sediment is eroded according to the above method (Fig. 9). The sediment activity values of each layer are 4.38%-33.84%, 0.32%-15.85%, 0.84%-26.39%, 0.17%-5.01%, 0.01%-64.42%, 0.01%-3.67%, 0.02%-17.17%, and 0.11%-38.15%, respectively (Fig. 9). The vertical sediment activity shows an overall trend of fluctuating and decreasing, with large fluctuations in the surface layers of 0-10 cm and 30-35 cm. However, the surface layer of the CSD is currently more stable and not very erodible (Section 4.1), and we derive the future erodibility of this area from the vertical sediment activity. The critical shear stress increases with depth in the study area because of sediment consolidation, so the sediment activity gradually decreases with depth, and at the same time, the active area decreases (Fig. 9). While the values in the 0-10 cm surface layer fluctuate more due to more disturbances, the values in the 30-35 cm layer fluctuate more due to fewer data points and higher randomness. Figure 6e shows that τ_b decreases with increasing water depth; thus, after the surface sediment is eroded, the water depth becomes deeper and the influence of τ_b is weakened. Moreover, as the sediment is eroded, its water content increases, and its critical shear stress may decrease as the seawater ingresses. Therefore, the sediment is not eroded in the vertical direction constantly, and sediment erosion in the vertical direction is in dynamic balance.
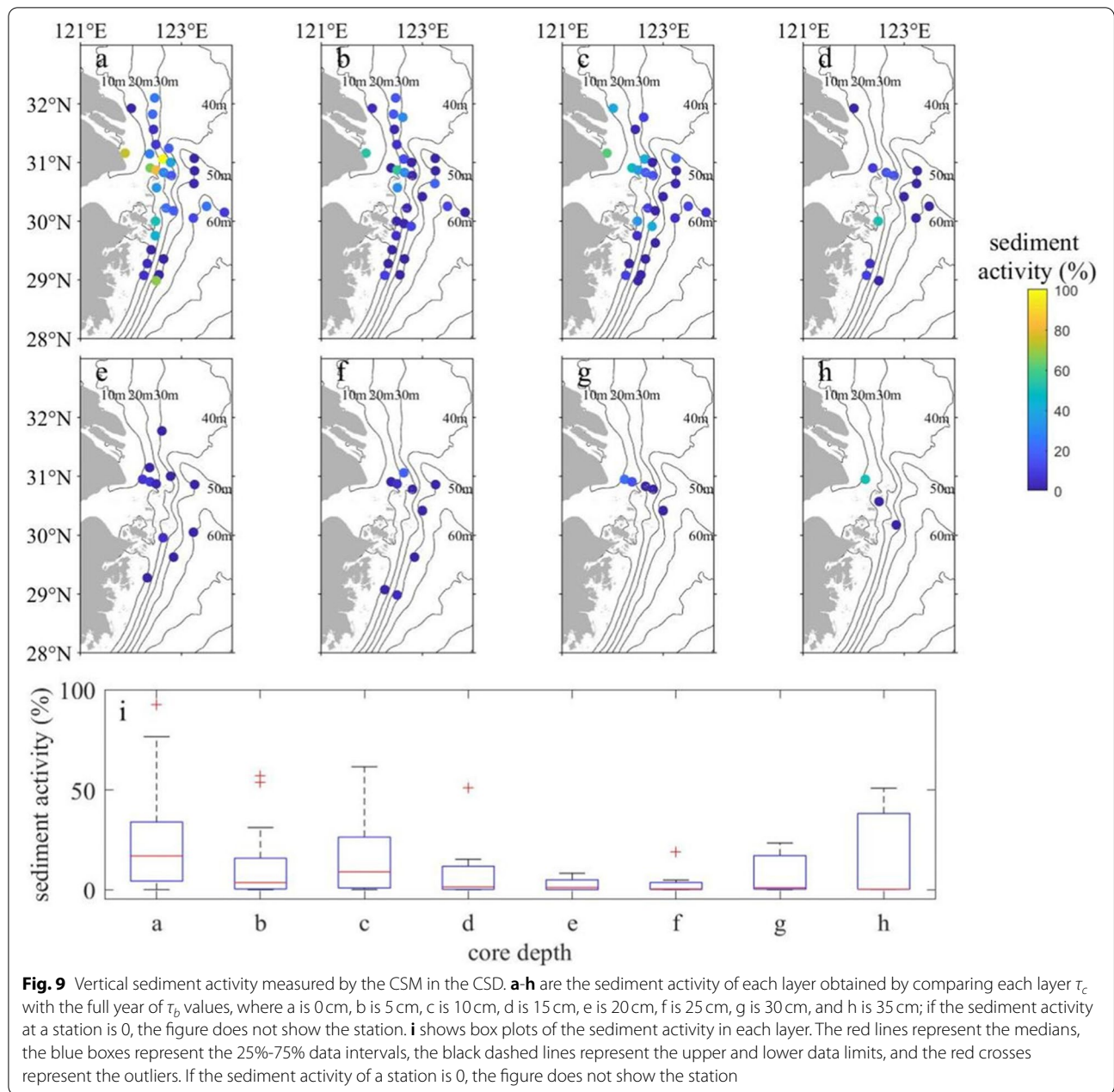
Floods and tropical cyclones can affect the development of the CSD due to their strong dynamic processes (Zhu et al. 2020). Swenson (2005) found that a reduction in the peak flood frequency and river runoff causes an increase in sediment transport, leading to the progradation of the CSD. Erosion occurs as a result of flood events and deposition follows via dry flows in the CSD, and erosion is prone to occur when the water

discharge > 60,000 m^3/s (Zhu et al. 2020). However, during the flood season of July–September, the occurrence of floods with such high flows is becoming less frequent due to the regulatory effect of the Three Gorges Dam closure (Dai et al. 2008), so the deep waters of the CSD remain in an accretion state. The East China Sea is more affected by tropical cyclones, and the hydrodynamics of storm surges triggered by tropical cyclones can affect areas with up to 40 m of water depth due to the fine grain size of the CSD, causing severe erosion or deposition in a short time (Dai et al. 2014b; Du et al. 2019). The sediment can be transported from deeper water to water that is shallower than −10 m under the influence of extreme storm surges, resulting in erosion in the deeper water and deposition in the shallower water of the CSD. For example, a series of typhoons in 2015 enhanced sediment transport from the deep-water scour zone offshore of the East China Sea, resulting in heavy deposition in the shallow water zone in 2013-2015. Resuspension occurred in the deep-water zone under the effect of storm surges to recharge the shallow water zone, the sediment load in the shallow water zone reached 237 Mt, and erosion occurred in the zone beyond a water depth of −14 m, resulting in the opposite pattern of erosion and accretion in the deep and shallow water zones (Chen et al. 2018). Because of global climate change, the tracks of tropical cyclones have shifted from the South China Sea to the East China Sea; the East China Sea will be affected by an increasing number of tropical cyclones in the future (Zhao et al. 2013), and the CSD may face increased short-term strong erosive conditions.

In summary, although the future erodibility of the CSD is low, there is still some risk of erosion in the future due to human activities and climate change, but the risk of large-scale erosion is not very likely.

4.3 Regional and global responses to human activities

Over the past half-century, the Changjiang River's sediment discharge has decreased by 80% due to the construction of > 50,000 dams and soil conservation (Yang et al. 2011), which has led to erosion in areas with water depths shallower than −10 m in the Changjiang mouth bar area (Li et al. 2015; Luan et al. 2021; Yang et al. 2011). This erosion may be exacerbated by continued dam construction in the future (Liu et al. 2014), but this area is less than one-fifth of the CSD and is not representative of the entire CSD. After the Three Gorges Dam (TGD) was established, even as the sediment load from the upper reaches declined, riverbed erosion along the 1000-km stretch between the TGD and the river mouth compensated for the loss and caused the grain size in this area to become coarser (Chen et al. 2010; Yang et al. 2017). Moreover, the slope of the shallow 10 m isobath area is

Xu *et al. Anthropocene Coasts*   (2022) 5:10

Page 12 of 15

Fig. 9 Vertical sediment activity measured by the CSM in the CSD. **a-h** are the sediment activity of each layer obtained by comparing each layer τ_c with the full year of τ_b values, where a is 0 cm, b is 5 cm, c is 10 cm, d is 15 cm, e is 20 cm, f is 25 cm, g is 30 cm, and h is 35 cm; if the sediment activity at a station is 0, the figure does not show the station. **i** shows box plots of the sediment activity in each layer. The red lines represent the medians, the blue boxes represent the 25%-75% data intervals, the black dashed lines represent the upper and lower data limits, and the red crosses represent the outliers. If the sediment activity of a station is 0, the figure does not show the station

significantly lower than the area between 10 m and 20 m, the steep slope is conducive to the formation of gravity flows to transport sediment from shallow water to deep water, the gentle shallow water area is susceptible to sediment resuspension by the combined current–wave action, and long-distance gravity flow transport occurs, which leads to deposition in the deep waters of the CSD (Wright and Friedrichs 2006; Dai et al. 2014a; Lowe 1982). Therefore, the deep-water area of the CSD is less affected by the reduced sediment discharge.

The CSD is not the only large system experiencing intensive human activities and substantial sediment load reduction. Almost all of the world's large rivers have been or are experiencing this threat (Wang et al. 2022). For example, the Mississippi River sediment load was reduced by more than half, and the cause for this substantial decrease in sediment has been attributed to the trapping characteristics of dams constructed on the muddy part of the Missouri River during the 1950s (Meade and Moody 2009). The sediment supply to the sea from the Nile River has nearly vanished

because of the sediment trapping effects of the New Aswan Dam constructed in 1964 and sediment deposition in the deltaic channel networks (Stanley 1996). Similar to the impact of sediment load reduction in the Changjiang River, they have triggered erosion in estuarine shoals and deltaic wetlands. The reductions were largely continuations of reductions owing to the initial wave of dam building in the mid-twentieth century. The additional impact of new dams on sediment flux to the oceans is diminishing (Dethier et al. 2022). Similar sediment load reductions have occurred in the Mekong River due to recent hydropower dam construction, triggering rapid erosion of the delta in areas shallower than 10 m isobaths (Anthony et al. 2015). The Yellow River, once the most sediment-laden river in the world, has experienced a rapid sediment flux reduction because of reforestation and reservoir construction (Wu et al. 2020). However, riverbed erosion has compensated for part of the loss, similar to the Changjiang River, which resulted in delta sediment coarsening (Liu et al. 2022). When the Water and Sediment Regulation Scheme is interrupted, the accretion–erosion conversion also does not exceed the 20 m isobaths (Wu et al. 2021).

In summary, river sediment load reduction has the greatest impact on the erosion of shorelines, wetlands, and subaqueous deltas shallower than the 10-20 m isobaths. The subaqueous deltas deeper than the 20 m isobath have a weak response to erosion under sediment load reduction.

5 Conclusion

This study discusses the relationship between the CSM-derived critical shear stress τ_{cr-m} and the empirical formula-derived critical shear stress τ_{cr-f} and derives the spatial distribution of the surface, as well as the vertical erodibility of the CSD. We give the present and future variations in the erodibility of the CSD, with the following main conclusions:

1) The surface critical shear stress values measured by the CSM vary from 1.11-2.25 N/m^2, and the surface critical shear stress values calculated by the empirical formula vary from 0.03-0.25 N/m^2. The empirical formula-derived critical shear stress relying only on grain size differs significantly from the CSM-derived critical shear stress. The CSM-derived critical shear stress is closer to the real situation of the sediment and better reflects the erodibility of the sediment. To analyze the erodibility, we prefer to use the CSM.

2) The sediment surface (0-10 cm) fluctuates greatly in areas with shallow water depths of 15 m and areas of 30~50 m because of the change in the bed shear stress and the shifting of the sand–mud boundary. The critical shear stress measured by the CSM tends to increase with depth due to sediment consolidation.

3) The southwestern and eastern areas of the CSD have low sediment activity (10.4% and 21.9%, respectively), while the central area has high sediment activity (43.9%). There are still some risks of erosion in the study area in the future due to human activities and climate change, but large-scale erosion is unlikely to occur.

Supplementary Information

The online version contains supplementary material available at https://doi.org/10.1007/s44218-022-00011-5.

Additional file 1: Fig. S1. Explicit Shields diagram in terms of dimensionless sediment diameter D_*. The minimum D_* represents sediments with a median grain size of 4 μm, cite from Guo (2020). **Fig. S2.** Main components of a CSM, cited from Wei et al., 2021a (1 compressed air cylinder, 2 compressed gas input port, 3 water storage chamber, 4 measurement chamber). **Fig. S3.** Verification of east-west flow velocity near the bottom (a) station A, (b) station B, (c) station C, (d) station D, (e) station E. **Fig. S4.** Verification of north-south flow velocity near the bottom (a) station A, (b) station B, (c) station C, (d) station D, (e) station E. **Fig. S5.** Spatial distribution of tidal currents in the study area in October 2019. (a) spring tide, (b) moderate tide, (c) neap tide, (d) maximum flood, (e) maximum ebb.

Authors' contributions
Chaoran Xu: Methodology, software, data curation, Writing-Original draft preparation. Dongyun Wei: Methodology, software, data curation. Yining Chen: Methodology, Writing – review & editing. Yang Yang: Methodology, Writing – review & editing Fan Zhang: Writing – review & editing. Yaping Wang: Writing – review & editing Jianjun Jia: Conceptualization, Methodology, Project administration, Writing – review & editing. The author(s) read and approved the final manuscript.

Availability of data and materials
The frst author, Mr. Chaoran Xu (cr_xu@outlook.com) can be contacted for access to the data.

Declarations

Competing interests
The authors declare no competing interests. The authors Yining Chen and Ya Ping Wang are members of the Editorial Board for Anthropocene Coasts. They were not involved in the journal's review of, or decisions related to, this manuscript. The authors have no other competing interests to disclose.

Author details
[1]State Key Laboratory of Estuarine and Coastal Research, School of Marine Sciences, East China Normal University, Shanghai 200241, China. [2]State Research Centre for Island Exploitation and Management, Second Institute of Oceanography, MNR, Hangzhou 310012, China. [3]School of Marine Science and Engineering, Nanjing Normal University, Nanjing 210046, China. [4]Key Laboratory of Ocean Space Resource Management Technology, MNR, Hangzhou 310012, China.

References

Amos CL, Bergamasco A, Umgiesser G, Cappucci S, Cloutier D, DeNat L, Flindt M, Bonardi M, Cristante S (2004) The stability of tidal flats in Venice Lagoon—the results of in-situ measurements using two benthic, annular flumes. J Mar Syst 51(1-4):211–241

Anthony EJ, Brunier G, Besset M, Goichot M, Dussouillez P, Nguyen VL (2015) Linking rapid erosion of the Mekong River delta to human activities. Sci Rep 5(1):14745

Carriquiry JD, Sánchez A, Camacho-Ibar VF (2001) Sedimentation in the northern Gulf of California after cessation of the Colorado River discharge. Sediment Geol 144(2001):37–62

Chen C, Beardsley RC, Cowles G, Qi J, Lai Z, Gao G (2006) An unstructured grid, finite-volume coastal ocean model: FVCOM user manual. Oceanography 19(1):78–89

Chen Y, Thompson CEL, Collins MB (2012) Saltmarsh creek bank stability: Bio-stabilisation and consolidation with depth. Cont Shelf Res 35:64–74

Chen Y, Wang H, Shi Y, Li B (2018) Characteristics and trends of morphological evolution of the Yangtze subaqueous delta during 1958—2015 (in Chinese). Adv Water Sci 29(3):314–321

Chen Z, Wang Z, Finlayson B, Chen J, Yin D (2010) Implications of flow control by the Three Gorges Dam on sediment and channel dynamics of the middle Yangtze (Changjiang) River, China. Geology 38(11):1043–1046

Chen Z, Xu K, Masataka W (2007) Dynamic hydrology and geomorphology of the Yangtze River. In: Geomorphology and management, pp 457–469

CWRC, 2021. Changjiang sediment bulletin 2020 (in Chinese)

Dade WB, Nowell ARM, Jummars PA (1992) Predicting erosion resistance of muds. Mar Geol 105(1-4):285–297

Dai Z, Du J, Li J, Li W, Chen J (2008) Runoff characteristics of the Changjiang River during 2006: effect of extreme drought and the impounding of the Three Gorges Dam. Geophys Res Lett 35(7):L07406

Dai Z, Fagherazzi S, Mei X, Chen J, Meng Y (2016) Linking the infilling of the north branch in the Changjiang (Yangtze) estuary to anthropogenic activities from 1958 to 2013. Mar Geol 379:1–12

Dai Z, Liu JT, Wei W, Chen J (2014b) Detection of the three gorges dam influence on the Changjiang (Yangtze River) submerged delta. Sci Rep 4(1):6600

Dai Z-J, Liu JT, Xie H-L, Shi W-Y (2014a) Sedimentation in the outer Hangzhou Bay, China: the influence of Changjiang sediment load. J Coast Res 298:1218–1225

Day JW, Agboola J, Chen Z, D'Elia C, Forbes DL, Giosan L, Kemp P, Kuenzer C, Lane RR, Ramachandran R, Syvitski J, Yañez-Arancibia A (2016) Approaches to defining deltaic sustainability in the 21st century. Estuar Coast Shelf Sci 183:275–291

Dethier EN, Renshaw CE, Magilligan FJ (2022) Rapid changes to global river suspended sediment flux by humans. Science 376(6600):1447–1452

Du J, Park K, Dellapenna TM, Clay JM (2019) Dramatic hydrodynamic and sedimentary responses in Galveston Bay and adjacent inner shelf to hurricane Harvey. Sci Total Environ 653:554–564

Fagherazzi S, Furbish DJ (2001) On the shape and widening of salt marsh creeks. J Geophys Res Oceans 106(1):991–1003

Gao S, Fang G, Yu K, Jia J (2001) Methodology for evaluating the stability of sandy seabed controlled by sediment movement, with an example of application(in Chinese). Stud Mar Sin 00:25–37

Gehrels WR (1999) Middle and Late Holocene sea-level changes in eastern Maine reconstructed from foraminiferal saltmarsh stratigraphy and AMS 14C dates on basal peat. Quat Res 52(3):350–359

Giosan L, Syvitski J, Constantinescu S, Day J (2014) Protect the world's deltas. Nature 516(7529):31–33

Grabowski RC, Droppo IG, Wharton G (2010) Estimation of critical shear stress from cohesive strength meter-derived erosion thresholds. Limnol Oceanogr Methods 8(12):678–685

Guo J (2020) Empirical model for shields diagram and its applications. J Hydraul Eng 146(6):04020038

Hori K, Saito Y, Zhao Q, Cheng X, Wang P, Sato Y, Li C (2001) Sedimentary facies and Holocene progradation rates of the Changjiang (Yangtze) delta, China. Geomorphology (Amsterdam, Netherlands) 41(2):233–248

Leeder M (1999) Sedimentology and sedimentary basins: From turbulence to tectonics. West Sussex: Blackwell Science, 137245–137246

Li B, Yan XX, He ZF, Chen Y, Zhang JH (2015) Impacts of the Three Gorges Dam on the bathymetric evolution of the Yangtze River Estuary (in Chinese). Chin Sci Bull 60(18):1735–1744

Liu JH, Yang SL, Zhu Q, Zhang J (2014) Controls on suspended sediment concentration profiles in the shallow and turbid Yangtze estuary. Cont Shelf Res:9096–9108

Liu L, Wang H, Yang Z, Fan Y, Wu X, Hu L, Bi N (2022) Coarsening of sediments from the Huanghe (Yellow River) delta-coast and its environmental implications. Geomorphology 401:108105

Liu X-L, Zheng J-W, Zhang H, Zhang S-T, Liu B-H, Shan H-X, Jia Y-G (2017) Sediment critical shear stress and geotechnical properties along the modern Yellow River Delta, China. Mar Georesour Geotechnol 36(8):875–882

Lowe DR (1982) Sediment gravity flows; II, depositional models with special reference to the deposits of high-density turbidity currents. J Sediment Res 52(1):279–297

Luan HL, Ding PX, Yang SL, Wang ZB (2021) Accretion-erosion conversion in the subaqueous Yangtze Delta in response to fluvial sediment decline. Geomorphology 382:107680

Luo XX, Yang SL, Wang RS, Zhang CY, Li P (2017) New evidence of Yangtze delta recession after closing of the three gorges dam. Sci Rep 7(1):41735

Mai Z, Zeng X, Wei X, Sun C, Niu J, Yan W, Du J, Sun Y, Cheng H (2022) Mangrove restoration promotes the anti-scouribility of the sediments by modifying inherent microbial community and extracellular polymeric substance. Sci Total Environ 811:152369

Maloney JM, Bentley SJ, Xu K, Obelcz J, Georgiou IY, Miner MD (2018) Mississippi River subaqueous delta is entering a stage of retrogradation. Mar Geol 400:12–23

Massey AC, Paul MA, Gehrels WR, Charman DJ (2006) Autocompaction in Holocene coastal back-barrier sediments from South Devon, Southwest England, UK. Mar Geol 226(3-4):225–241

Meade RH, Moody JA (2009) Causes for the decline of suspended-sediment discharge in the Mississippi River system, 1940-2007. Hydrol Process 24(1):35–49

Milliman JD, Farnsworth KL (2011) River discharge to the coastal ocean: a global synthesis

Milliman JD, Huang-ting S, Zuo-sheng Y, Mead RH (1985) Transport and deposition of river sediment in the Changjiang estuary and adjacent continental shelf. Cont Shelf Res 4(1-2):37–45

Sanford LP (2008) Modeling a dynamically varying mixed sediment bed with erosion, deposition, bioturbation, consolidation, and armoring. Comput Geosci 34(10):1263–1283

Shi BW, Yang SL, Wang YP, Yu Q, Li ML (2014) Intratidal erosion and deposition rates inferred from field observations of hydrodynamic and sedimentary processes: a case study of a mudflat–saltmarsh transition at the Yangtze delta front. Cont Shelf Res 90:109–116

Soulsby RL (1997) Dynamics of marine sands. Thomas Telford Publications, London, pp 1–250

Stanley DJ (1996) Nile delta: extreme case of sediment entrapment on a delta plain and consequent coastal land loss. Mar Geol 129(3):189–195

Swenson JB (2005) Fluvial and marine controls on combined subaerial and subaqueous delta progradation: Morphodynamic modeling of compound-clinoform development. J Geophys Res 110(2):1–16

Syvitski JP, Vorosmarty CJ, Kettner AJ, Green P (2005) Impact of humans on the flux of terrestrial sediment to the global coastal ocean. Science 308(5720):376–380

Syvitski JPM, Kettner AJ, Overeem I, Hutton EWH, Hannon MT, Brakenridge GR, Day J, Vörösmarty C, Saito Y, Giosan L, Nicholls RJ (2009) Sinking deltas due to human activities. Nat Geosci 2(10):681–686

Syvitski JPM, Saito Y (2007) Morphodynamics of deltas under the influence of humans. Glob Planet Chang 57(3-4):261–282

Tolhurst TJ, Riethmuller R, Paterson DM (2000) In situ versus laboratory analysis of sediment stability from intertidal mudfats. Cont Shelf Res 20(10):1317–1334

Tolhursta TJ, Blacka KS, Shaylerb SA, Patersona DM, Mathera S, Blackc I, Baker K (1999) Measuring the in situ Erosion shear stress of intertidal sediments with the cohesive strength meter (CSM). Estuar Coast Shelf Sci 49(2):281–294

Vardy S, Saunders JE, Tolhurst TJ, Davies PA, Paterson DM (2007) Calibration of the high-pressure cohesive strength meter (CSM). Cont Shelf Res 27(8):1190–1199

Wang C, Zhang C, Wang Y, Jia G, Wang Y, Zhu C, Yu Q, Zou X (2022) Anthropogenic perturbations to the fate of terrestrial organic matter in a river-dominated marginal sea. Geochim Cosmochim Acta 333:242–262

Xu *et al. Anthropocene Coasts* *(2022) 5:10*

Page 15 of 15

Wei D (2021) Sediment activity in the Changjiang River subaqueous delta (in Chinese). East China Normal University, Shanghai

Wei D, Chen Y, Xu C, Xue C, Wang M, Jia J (2021) On the sediment activity of the Changjiang River Submerged Delta with the background of reduced sediment flux into the sea (in Chinese). Resour Environ Yangtze Basin 30(11):2630–2640

Whitehouse RJS, Bassoullet P, Dyer KR, Mitchener HJ, Roberts W (2000) The influence of bedforms on flow and sediment transport over intertidal mudflats. Cont Shelf Res 20(10):1099–1124

Widdows J, Friend PL, Bale AJ, Brinsley MD, Pope ND, Thompson CEL (2007) Inter-comparison between five devices for determining erodability of intertidal sediments. Cont Shelf Res 27(8):1174–1189

Wright LD (1977) Sediment transport and deposition at river mouths: a synthesis. Geol Soc Am Bull 88(6):857–868

Wright LD, Friedrichs CT (2006) Gravity-driven sediment transport on continental shelves: a status report. Cont Shelf Res 26(17-18):2092–2107

Wu X, Fan Y, Wang H, Bi N, Yang Z, Xu C (2021) Geomorphological responses of the lower river channel and delta to interruption of reservoir regulation in the Yellow River (in Chinese). Chin Sci Bull 66(23):3059–3070

Wu X, Wang H, Bi N, Saito Y, Xu J, Zhang Y, Lu T, Cong S, Yang Z (2020) Climate and human battle for dominance over the Yellow River's sediment discharge: from the mid-Holocene to the Anthropocene. Mar Geol 425:106188

Xue C, Sheng H, Dongyun W, Yang Y, Yaping W, JIia J (2020) Dry bulk density analysis for inner shelf sediments of the East China Sea and its sedimentary implications(in Chinese). Oceanol Limnol Sin 51(5):1093–1107

Yang HF, Yang SL, Li BC, Wang YP, Wang JZ, Zhang ZL, Xu KH, Huang YG, Shi BW, Zhang WX (2021) Different fates of the Yangtze and Mississippi deltaic wetlands under similar riverine sediment decline and sea-level rise. Geomorphology 381:107646

Yang HF, Yang SL, Meng Y, Xu KH, Luo XX, Wu CS, Shi BW (2018) Recent coarsening of sediments on the southern Yangtze subaqueous delta front: a response to river damming. Cont Shelf Res 155:45–51

Yang HF, Yang SL, Xu KH, Wu H, Shi BW, Zhu Q, Zhang WX, Yang Z (2017) Erosion potential of the Yangtze Delta under sediment starvation and climate change. Sci Rep 7(1):10535

Yang SL, Milliman JD, Li P, Xu K (2011) 50,000 dams later: Erosion of the Yangtze River and its delta. Glob Planet Chang 75(1-2):14–20

Yang SL, Xu KH, Milliman JD, Yang HF, Wu CS (2015) Decline of Yangtze River water and sediment discharge: impact from natural and anthropogenic changes. Sci Rep 5(1):12581

Yang Y, Gao S, Wang YP, Jia J, Xiong J, Zhou L (2019) Revisiting the problem of sediment motion threshold. Cont Shelf Res 187:103960

Yun C (2004) Recent evolution of the Yangtze estuary and its mechanisms (in Chinese). China Ocean Press, Beijing

Zhao H, Wu L, Wang R (2013) Decadal variations of intense tropical cyclones over the western North Pacific during 1948–2010. Adv Atmos Sci 31(1):57–65

Zhu B, Li Y, Yue Y, Yang Y, Liang E, Zhang C, Borthwick AGL (2020) Alternate erosion and deposition in the Yangtze estuary and the future change. J Geogr Sci 30(1):145–163

Publisher's Note